

## Detection of geohazards in the Bailong River Basin using synthetic aperture radar interferometry

**Abstract** Fifty-five descending images from the ENVISAT satellite were processed using the small baseline subset (SBAS) method to derive the spatial and temporal ground deformation of the Bailong River Basin between 2003 and 2010. The basin is one of the most severely landslide- and debris flow-affected areas of China. As a result, 104 sites with high deformation areas were identified. Interferometric Synthetic Aperture Radar (InSAR) analysis was combined with landslide inventory data and field surveys, and anomalous areas were classified into three main types: landslide; debris; and subsidence. Displacement rates up to 35 mm/yr were evaluated away from the sensor along a line-of-sight (LOS) direction. The results gained should allow a more accurate prediction and monitoring of landslides, debris, and subsidence; further, they demonstrate the capability of the SBAS method to analyze any displacement effect and identify dangerous and uninhabitable areas in the basin. The small baseline subset method can thus contribute to the prediction and prevention of geohazards in the area.

**Keywords** Small baseline subset · Bailong River Basin · Anomalous area · Geohazard

### Introduction

The Bailong River Basin is one of the regions in China that is most susceptible to mountainous disasters. Tectonic movement, soft/crushed strata, and active faults control the general distribution and frequency of geohazards such as landslides, debris flows and subsidence. The Wenchuan earthquake of May 12th 2008 had a serious impact upon rock and soil structures, resulting in more than 15,000 landslides and debris flows. There were multiple fatalities; more than one million people living in the region remain threatened by the potential occurrence of such geohazards (Bai et al. 2012; 2013). The increasing frequency of such geohazard events has been exerting serious impacts upon local people and the economic development of the region.

In recent years, many qualitative and quantitative mapping techniques have been created to investigate the area most sensitive to future geohazards; these methods have included field surveys, risk assessments (Dai et al. 2002), and susceptibility assessments (van Westen et al. 2008). In the Bailong River Basin, different models were compared and combined for optimal landslide susceptibility zonation (Chen et al. 2014); the susceptibility assessment method was applied to describe the maximum likelihood of landslides in Zhouqu segment (Bai et al. 2012) and Wudu County (Bai et al. 2013). But all these methods include uncertainties and limitations in their ability to accurately determine the spatial and temporal risks inherent in areas sensitive to geohazards. It is necessary to apply more efficient techniques to gain more accurate results from mapping dangerous areas; this will support a more effective management of geohazards and enable safer land planning.

Surface displacement detecting and monitoring are critical to the identification of unstable areas and to the consequent reduction in geohazard damage. In recent years, InSAR data has provided a complementary method for detecting ground deformation (Michoud et al. 2015; Motagh et al. 2014; Schlögel et al. 2015). The technique has high spatial and temporal advantages compared to traditional detection methods such as GPS, optical remote sensing, geological, and geophysical methods (Massonnet and Feigl 1998). Various InSAR techniques have been developed to investigate ground deformation, such as the differential InSAR method (Gabriel et al. 1989; Li et al. 2004), the persistent scatterer InSAR method (Ferretti et al. 2000, 2001; Kampes and Adam 2003), and the small baseline subset (SBAS) method (Berardino et al. 2002; Casu et al. 2006). All the aforementioned methods have been employed in geohazard studies to detect surface deformation, including earthquakes (Massonnet and Feigl 1998), subsidence (Liu et al. 2010; Stramondo et al. 2008), volcanic activity (Hooper et al. 2004; Peltier et al. 2010), and landslides (Akbarimehr et al. 2013; Ciampalini et al. 2014; Zhao et al. 2012). The persistent scatterer InSAR and SBAS techniques have both overcome the limitations (temporal and spatial decorrelation) inherent in differential InSAR. In addition, the SBAS technique is more suited to rugged terrain which lacks sufficient persistent scatterers (Hooper et al. 2012). However, in a region with a rugged terrain and dense vegetation coverage, there are very limited applications of SBAS techniques to monitor different geohazards at a large scale.

In this paper, and for the first time, we analyze the deformation of rugged terrain, and map dangerous areas, on a basin scale using the SBAS method (StaMPS/MTI) (Hooper 2008) vis-à-vis the Bailong River Basin. The main objectives of the paper are: (1) demonstrating the reliability of the SBAS technique in detecting and monitoring geohazards, (2) detecting ground deformation on a regional scale and interpreting such deformation using field surveys, allowing areas with high displacement rates to be identified as dangerous areas. This will provide a foundation for the reduction and possible prevention of geohazards.

### Geomorphological and geological settings

The Bailong River Basin covers an area of 18,500 km<sup>2</sup> in southern Gansu Province, China. The basin, located in the western tectonic zone of the Qinling Mountains, is surrounded by the Qinghai-Tibet Plateau (TP), the Chinese Loess Plateau (CLP), and the Sichuan Basin, with elevations varying from 568 to 4866 m asl. It is affected by the intense tectonic uplift of the TP, which dominates the area's landforms. The Bailong River is a secondary tributary of the Yangtze River; its basin is one of the regions of China most severely affected by landslides and debris flows. Vast amounts of loose material are transported via the Bailong River into the Yangtze itself.

The landforms of this region are controlled by the Bailong River Fault Zone. The area is characterized by an interlocking distributive pattern of mountains, valleys, and sub-basins. Gentle river valley gradients contrast with steep mountainsides. Within

the basin are outcrops of phyllites, sandy slates, sandstones, and limestones of the Silurian period; limestones, dolomites, slates, and phyllites of the Devonian period; limestones, dolomites, and entrained phyllites, slates, and shale of Carboniferous and Permian periods; conglomerates, mudstones, siltstones, and shales of the Triassic and Jurassic periods; and sandstones, shales, and mudstones of the Cretaceous period (Fig. 1). These rocks are mostly overlain by Quaternary sediments (loess, clays, and gravels). Landslides in this area containing loose slope deposits and heavily weathered rocks are triggered by precipitation, earthquakes, and human activity.

As the population of the Bailong River Basin has grown, its economy has rapidly developed; unregulated human activities have consequently destabilized the area's slopes. Improperly engineered road construction has not included slope regulation, stabilization, and management, especially at the toes of slopes. Reclamation of land for cultivation has increased the risk of flooding whilst reducing water retention rates. Water extraction for irrigation has further weakened the structure of the soil. As a result, landslides in and around urban areas have become frequent.

### Multi-temporal deformation mapping

#### Input data

This study is based on a series of ENVISAT SAR images from descending satellite C-band tracks covering the Bailong River Basin between November 2003 and September 2010 (Fig. 2). The ENVISAT image sets are shown in Table 1. Each image covers 100×100 km<sup>2</sup>. We used a digital elevation model (DEM) with a resolution of 90 m, obtained by the Shuttle Radar Topography Mission (SRTM). Due to the decorrelation caused by layover and shadows in mountainous regions, we selected areas of less rugged terrain in populated valleys as our study areas (Fig. 2).

All 55 descending track images were processed to generate 93 interferograms with perpendicular baseline thresholds of Bperp (perpendicular baseline) <600 m and temporal baseline thresholds of Btemp (temporal baseline) <600d (Fig. 3).

#### Methodology

In this study, the SBAS technique proposed by Hooper (2008) and the 3D-phase unwrapping algorithm proposed by Hooper and Zebker (2007) were selected to obtain deformation results.

The first step in the method included co-registration, geometric phase correction, geocoding, and interferogram formation. The Delft Object-Oriented Radar Interferometric Software (DORIS) developed by the Delft Institute of Earth Observation and Space Systems was used to process co-registration and interferograms generation.

The second step involved the identification of slowly-decorrelating filtered phase (SDFP) pixels and phase unwrapping. We selected initial SDFP pixel candidates using amplitude stability analysis. The amplitude dispersion index in Eq. (1),  $D_A$ , as defined by Ferretti et al. (2001), was used to reject those least likely to be SDFP pixels, thus:

$$D_A = \frac{\sigma_A}{\mu_A} \quad (1)$$

Where  $\sigma_A$  and  $\mu_A$  are the standard deviation and the mean of a series of amplitude values, respectively. We set 0.6 as the threshold for obtaining initial SDFP pixels. These pixels had to include a ground displacement phase, a temporal change in atmospheric delay, orbital inaccuracies and a spatially-correlated height error.

An estimate of the decorrelation noise for a pixel, similar to coherence magnitude, was made using Eq. (2), then analyzed to identify SDFP pixels among the candidate pixels:

$$\gamma_x = \frac{1}{N} \left| \sum_{i=1}^N \exp \left\{ \sqrt{-1} \left( \psi_{x,i} - \tilde{\psi}_{x,i} - \Delta \tilde{\Phi}_{\theta,x,i}^u \right) \right\} \right| \quad (2)$$

Where  $\psi_{x,i}$  is the wrapped phase of pixel  $x$  in the  $i$ th interferogram,  $\tilde{\psi}_{x,i}$  is the estimate of the spatially-correlated terms,  $\Delta \tilde{\Phi}_{\theta,x,i}^u$  is the estimate of the spatially-uncorrelated look-angle error term, and  $N$  is the number of interferograms. After SDFP pixel selection, 3D-phase unwrapping algorithms as described by Hooper and Zebker (2007) were chosen to obtain real displacement after correction for the spatially-uncorrelated look-angle (SULA) error (DEM error).

Finally, any remaining spatially-correlated noise (atmospheric and orbital errors) was estimated and removed using high-pass filtering in time subsequent to low-pass filtering in space. The essential deformation was then generated after subtracting these noises.

### Results and discussion

Since the majority of the basin being a rural environment with its consequent vegetation cover, high slope inclination, and unsuitable orientation, most of the region has no radar coverage (Colombo et al. 2006), single descending acquisition data therefore leads to an absence of information on movement on NE-facing slopes (Meisina et al. 2008). Using satellite data, mean velocity maps of the Bailong River Basin were constructed (Fig. 4). The velocity was extracted along the line-of-sight (LOS) of the satellite, which is 23° on average from the vertical. Negative values represent the ground motion away from the LOS, while positive values represent movement towards the satellite. High deformation rates were located around Banzang and Xibugu villages and Zhouqu County at the upper reaches; Wudu County and Jiaogong and Majie towns at the middle reaches; and Jugan Town and Zhangjiaba Village at the down reaches. According to the precision of technique (Meisina et al. 2008; Colesanti and Wasowski 2004), the minimum velocity of ±2 mm/yr, considered as a real deformation, is determined by using the calculated standard deviation of velocity of the whole region (Hanssen 2005). The areas with displacement rates over 2 mm/yr are categorized as the "anomalous areas". More than 100 anomalous areas were identified in the Bailong River Basin. The size of the detected anomalous slope cell ranged from about 0.03 km<sup>2</sup> to more than 7 km<sup>2</sup>. The areas with the most significant rates of deformation were concentrated around counties like Zhouqu and Wudu, close to faults or located on soft bedrock (Figs. 1, 4). A field survey was conducted on the anomalous areas we selected, based on SDFP pixel distributions and interviews with local inhabitants.

A combination of field survey and landslide inventory data identified the causes of the deformation of anomalous areas as being related to: landslides; potential landslides; the movement of debris, and subsidence due to soft soil dissolution and/or consolidation of the soil-based foundations of buildings.

#### Landslides

Landslides occur frequently throughout the Bailong River Basin. Slope failures and human casualties are frequently reported. Landslides are caused by weakened geological strata and strong triggers (e.g., precipitation and earthquakes). InSAR detection and field

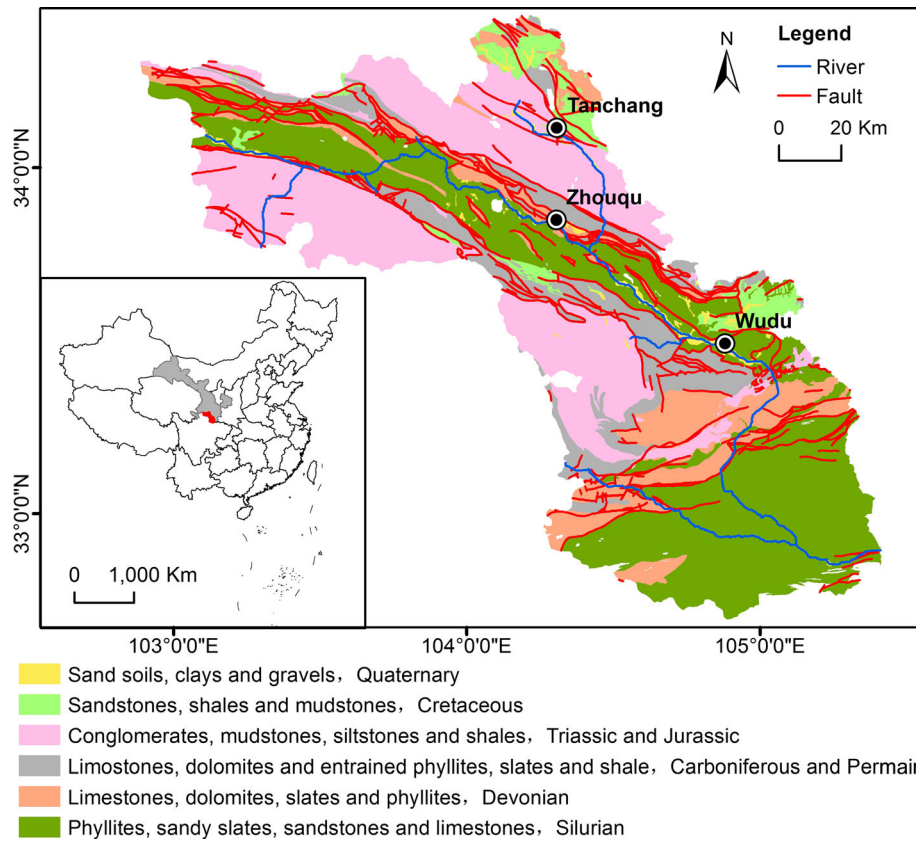


**Fig. 1** Geological map of the Bailong River Basin

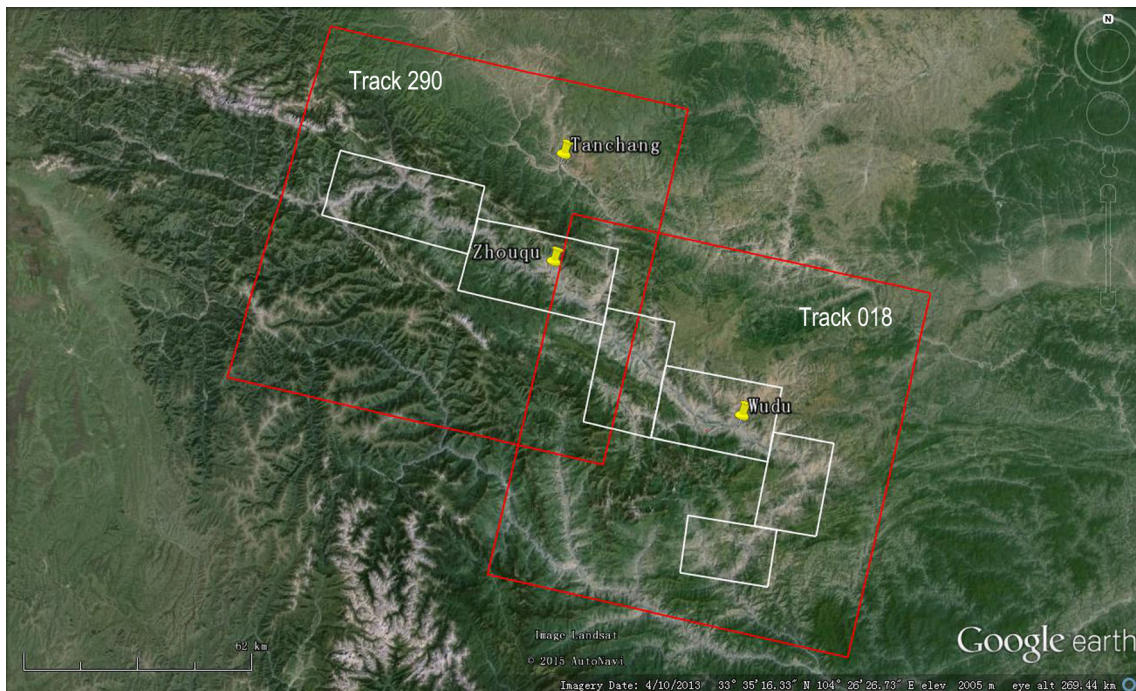


**Fig. 2** Location of the research area as covered by satellite image tracks 290 and 018. The *red rectangles* represent the areas covered by ENVISAT descending images. The *white rectangles* represent the study area



**Table 1** ENVISAT data for the Bailong River Basin

Track 290	Acq.date	Track 018	Acq. date
1	06 Aug 2007	1	26 Nov 2003
2	24 Dec 2007	2	19 May 2004
3	03 Mar 2008	3	23 Jun 2004
4	12 May 2008	4	01 Sep 2004
5	21 Jul 2008	5	15 Dec 2004
6	25 Aug 2008	6	23 Feb 2005
7	29 Sep 2008	7	08 Feb 2006
8	03 Nov 2008	8	28 May 2008
9	08 Dec 2008	9	06 Aug 2008
10	12 Jan 2009	10	10 Sep 2008
11	16 Feb 2009	11	15 Oct 2008
12	23 Mar 2009	12	19 Nov 2008
13	27 Apr 2009	13	24 Dec 2008
14	01 Jun 2009	14	28 Jan 2009
15	06 Jul 2009	15	04 Mar 2009
16	14 Sep 2009	16	08 Apr 2009
17	19 Oct 2009	17	13 May 2009
18	23 Nov 2009	18	22 Jul 2009
19	28 Dec 2009	19	30 Sep 2009
20	01 Feb 2010	20	04 Nov 2009
21	08 Mar 2010	21	09 Dec 2009
22	12 Apr 2010	22	13 Jan 2010
23	17 May 2010	23	17 Feb 2010
24	21 Jun 2010	24	24 Mar 2010
25	26 Jul 2010	25	28 Apr 2010
26	30 Aug 2010	26	02 Jun 2010
		27	07 Jul 2010
		28	11 Aug 2010
		29	15 Sep 2010

surveys confirmed that old landslide bodies had been carried at high velocities along the LOS. These old landslides were likely triggered by marked fault activity and rainfall; SBAS results confirmed that such events were widespread and located very close to tectonic faults. All landslides covered an area  $>0.2 \text{ km}^2$ . Most landslides were reactivated in successive years; landslides thus represent a serious risk to the Bailong River Basin. Numerous giant slow-moving landslides with large volumes over  $1,000,000 \text{ m}^3$  have already been observed reactivating around the Zhouqu segment (Bai et al. 2012; Dijkstra et al. 2012; Jiang and Wen 2014). These landslides tend to cause serious damage to facilities; the instability of the terrain can also dam rivers.

#### The Nanyu landslide

The Nanyu landslide is made up of a series of complex slope movements with extending over a total surface area of  $4.2 \text{ km}^2$ , next to the Bailong River. The landslide is an old fault-crushing

landslide; the most recent mass slide occurred in 1991 which blocked the Bailong River. The slope is 700 m at its widest, and 3300 m long. The sliding body consists of carbonaceous phyllite, limestone, slate rock fragments, and proluvial deposits. A spring rising through the landslide's body, combined with heavy rainfall, has induced recent landslide activity. Buildings have been erected, and land cultivated on the landslide's gentler slopes. Figure 5 shows the landslide's mean LOS deformation rates and field survey results. The average LOS velocity ranged from 0 to 35 mm/yr. The maximum deformation rate occurs in the central to lower part of the landslide corresponding to the multiple cracks shown in Fig. 5c. Severe deformation has broken the concrete retaining wall near the road (Fig. 5d). For the left and right sectors of the landslide, movement is associated with lower deformation rates. Figure 5b shows a displacement time series for representative pixels (for location, see Fig. 5a). Differences in the three time series

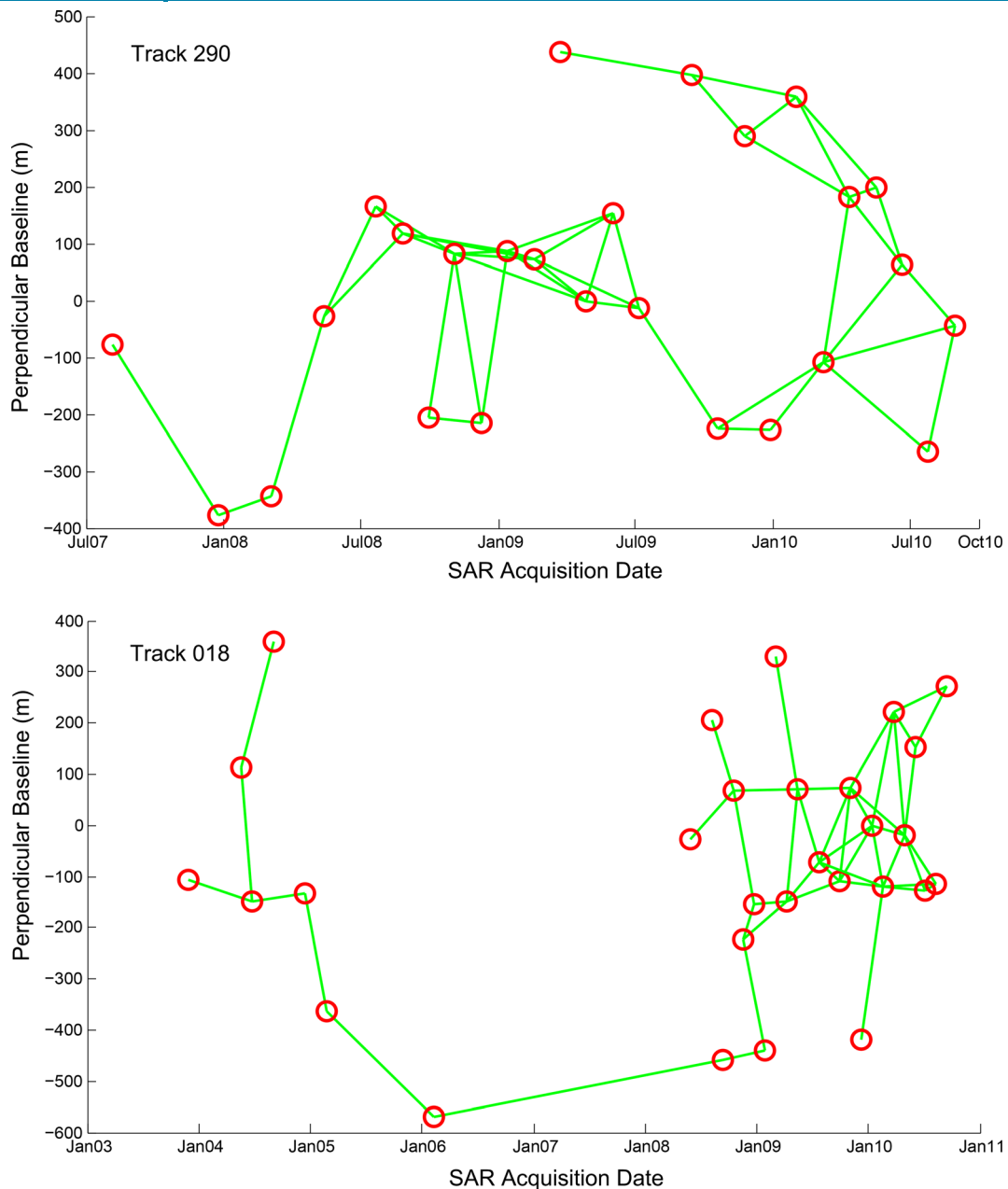


**Fig. 3** Spatial-temporal baselines of the generated interferograms. *Circles* represent InSAR images; the *lines* represent the interferometric pairs

suggest that the movements of three sectors are not highly correlated. The different sectors of the landslide exhibit various deformation rates because of their different gradients and human activities. Field surveys indicate many cracks were developed in the landslide, which is covered by rock fragments (Fig. 5c). The main causes of high landslide deformation rates may be continuous fault activity, heavy rainfall and weak strata. Human activity is also an important cause of landslide deformation.

#### The Xieliupo landslide

The Xieliupo landslide, 2700 m in length, is located on the SW-facing bank of the Bailong River along the Pingding-Huama Fault Zone. The general direction of slide is 285°, and its slope gradient varies from 20° to 45°. The landslide's body consists of soft phyllite, slate

and overlain Quaternary loess. This landslide has been active for several decades; 5 m of slip occurred after the Wenchuan earthquake on May 12, 2008. A highly shattered fault zone, very active tectonic activities, and precipitation are the principal landslide slippage triggers. Figure 6 shows deformation velocity along the LOS and the field survey results. However, the shadow coming from an absence of buildings and rugged terrain around the landslide reduces the number of the SDFP pixels. Deformation with a mean LOS velocity >30 mm/yr was detected on the lower sector of the landslide. Many large cracks were found in this area during the course of field surveys (Fig. 6c, d). But at the back (scarp) of the landslide, a lower deformation rate than for the lower sector indicated that the landslide was partly reactivating. Analysis of the deformation time series indicates that the movement of the landslide is non-significantly

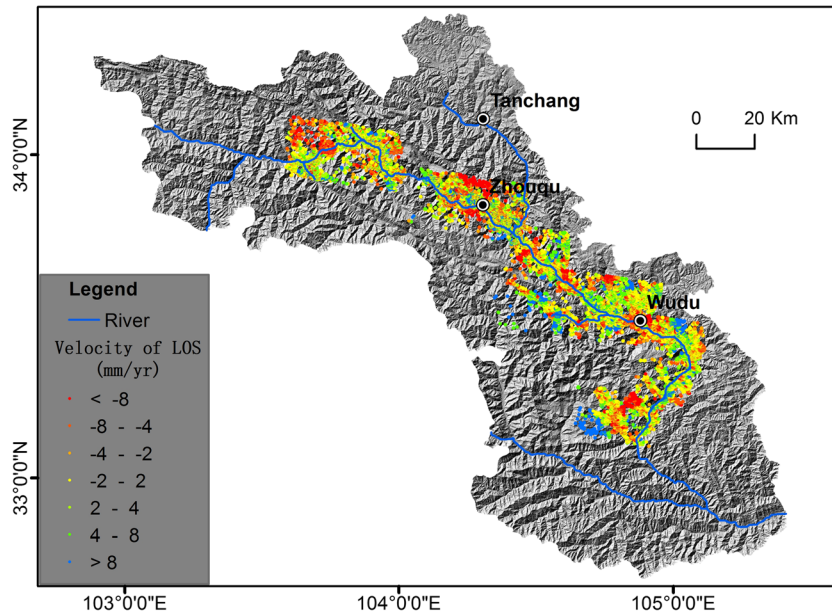


**Fig. 4** SBAS technique results

corresponding to rainfall due to the deep-seated slip surface and the hysteresis effect of rainfall infiltration (Fig. 6b).

#### The Suertou landslide

The Suertou landslide is a large-scale, fault-crushing slope located in the west of Zhouqu County. The widest part of the slope is 700 m, and it is 3300 m long. The direction of slide is  $133^\circ$  and the thickness of the landslide body ranges from 20 to 100 m. The sliding body consists of grey clayey soil with carbonate rock fragments, and dark grey clayey soil with carbonaceous slate rock fragments; the bedrock is carbonaceous slate cataclastite (Jiang and Wen 2014). Figure 7 shows a deformation map and the results of field surveys of the

slope. Due to the slope facing east and the extensive area of cultivated land, fewer SDFP pixels could be identified on the slope. However, higher deformation rates  $>20$  mm/yr were detected in buildings constructed in the top and lower buildings of landslide (Fig. 7a). Many of the surveyed buildings evinced damage, with cracks in their walls and the streets alongside them, corresponding to movement of the landslide (Fig. 7c, d). Figure 7b gives a time series for the points selected in the lower and back sectors of the landslide. Coincident deformation characteristics indicate that the whole landslide has reactivated over the years covered by this study. An active fault, heavy rainfall and human activity all trigger slope displacement.

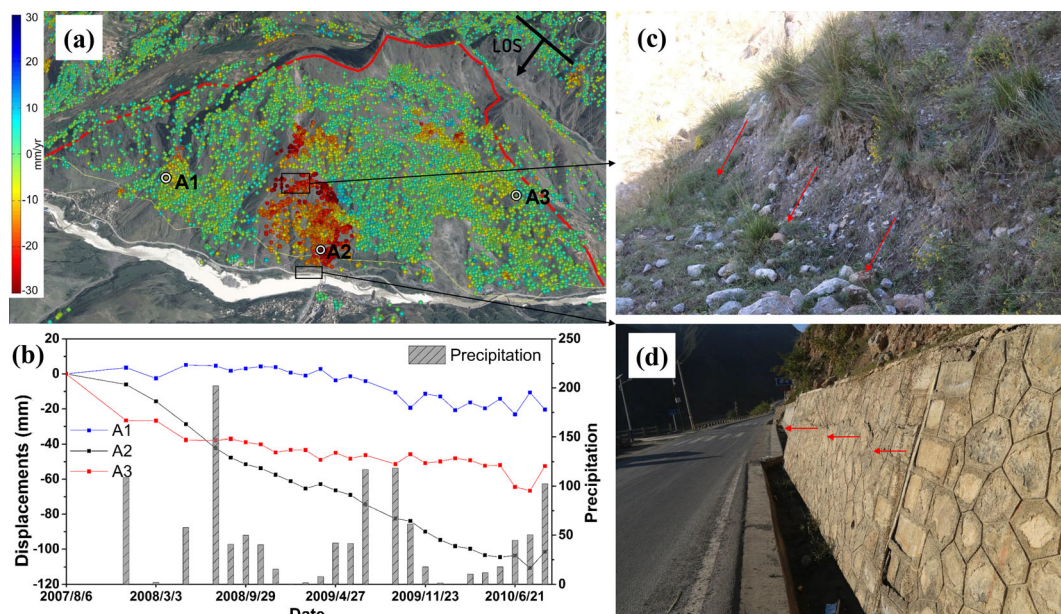


**Fig. 5** Displacement rates and damage, Nanyu landslide. (a) Mean LOS displacement rates for SDFP pixels superimposed on Google Earth map; (b) Displacement time series for representative pixels, for Points A1, A2 and A3; (c, d) Examples of cracks and damage in the retaining wall discovered during field surveys of the Nanyu landslide site



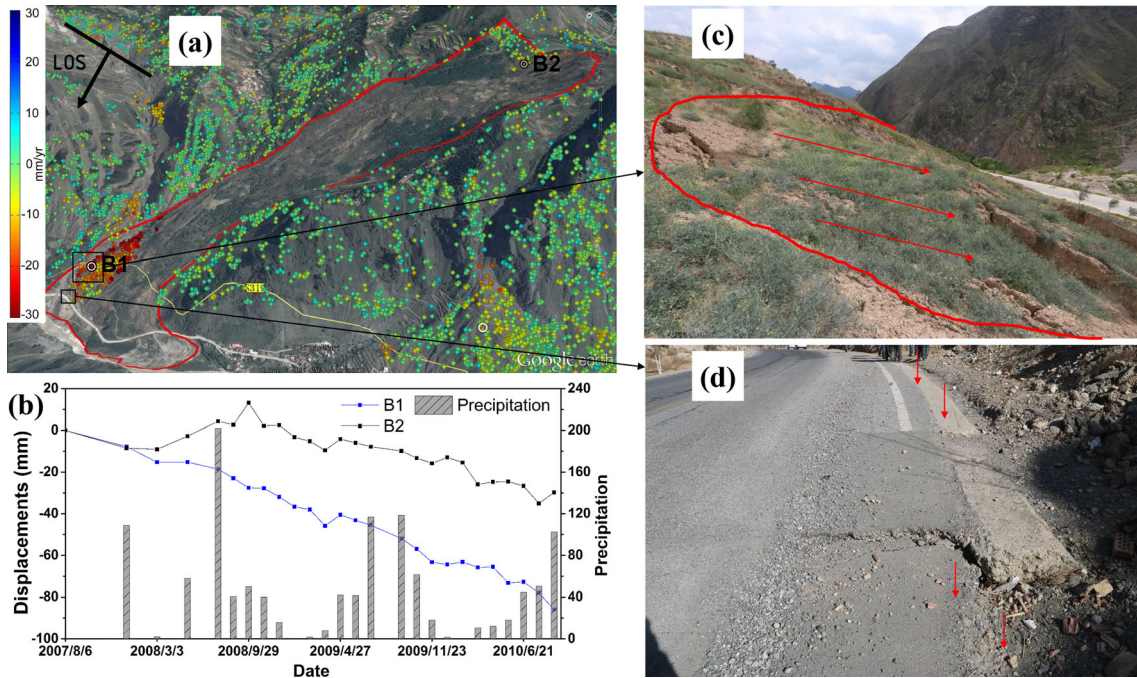


**Fig. 6** Displacement rates and damage, Xieliupo landslide. (a) Mean LOS displacement rates for SDFP pixels, superimposed on a Google Earth map; (b) Displacement time series for representative pixels, for Points B1 and B2; (c, d) Examples of cracks and damage to the road discovered during field surveys of the Xieliupo landslide site

#### Potential landslides

Using the SBAS technique and field surveys to detect deformation, it was established that many slopes possessing high deformation rates which were not classified as landslides prior to InSAR acquisition are, in fact, presently unstable. The scale of the cracks developing on the bodies of the slopes indicates the potential risk.

The slopes all consist of upper loess and/or colluvium deposits, combined with soft lower bedrock (e.g., phyllite, slate, sandstone, mudstone etc.). Human reclamation is one of the major triggers of slope failure in these areas. Figure 8 shows an example of a slope in Wudu County rendered unstable by road construction, closer to Wenchuan than to Zhouqu. Manual excavation of the hillside

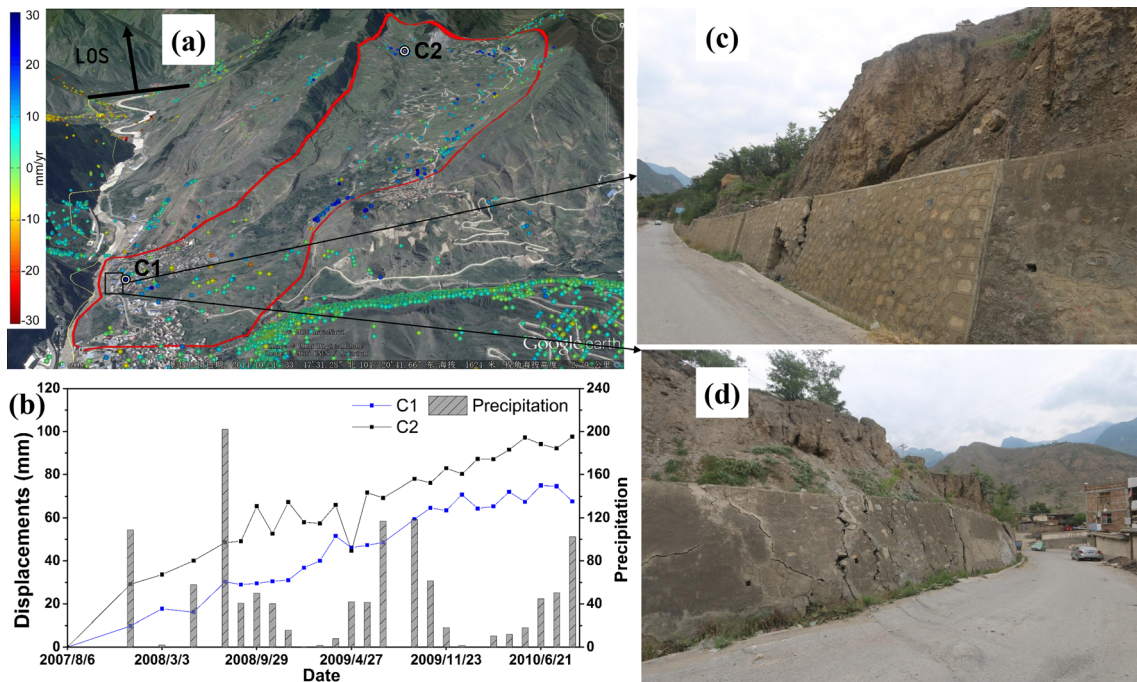


**Fig. 7** Displacement rates and damage, Suoertou landslide. (a) Mean LOS displacement rates for SDFP pixels, superimposed on a Google Earth map; (b) Displacement time series for representative pixels, for Points C1 and C2; (c, d) Examples of crack and damage to the road discovered during field surveys of the Suoertou landslide site



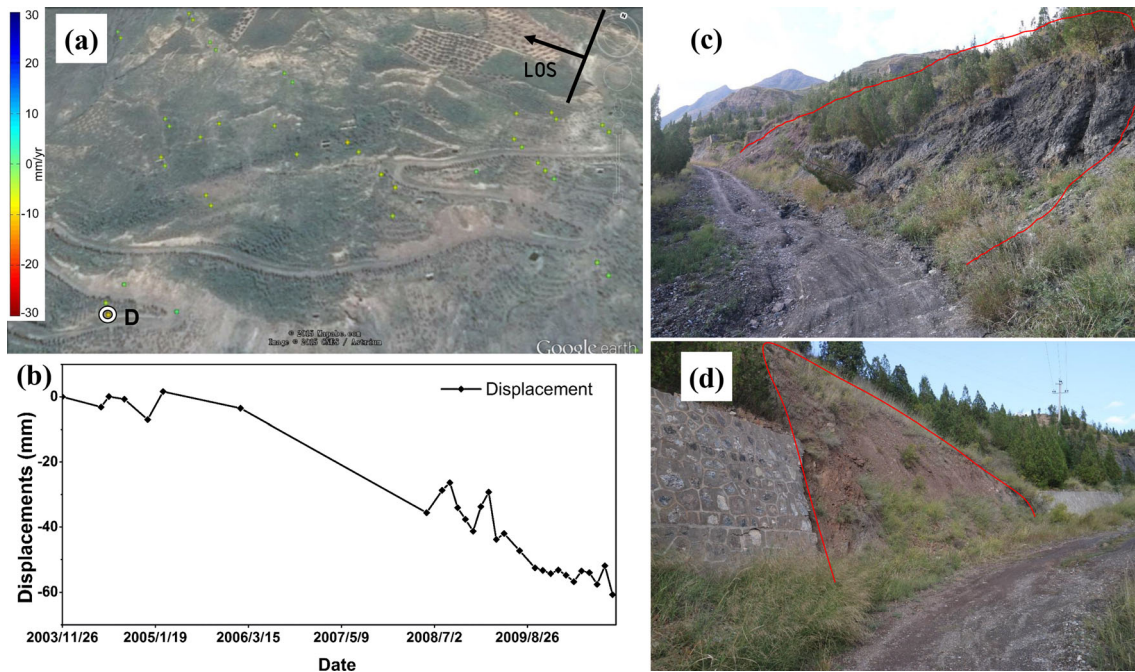


**Fig. 8** Displacement rates and damage caused by road construction. (a) Mean LOS displacement rates for SDFP pixels superimposed on Google Earth map; (b) Displacement time series for representative pixels, for Point D; (c, d) Examples of damage to the road discovered during field surveys

aerated the slope foot. Following periods of intense rainfall and an inherent weakness and instability in the soil, many cracks have now developed, leading to an imminent risk of landslides. Figure 8b shows a displacement time series for the slope's representative SDFP pixels. Higher mean deformation rates were recorded following the Wenchuan earthquake. Figure 8c and d show the roadside damage illustrated in Figure 8a. Frequent subsidence

has impinged upon the road and poses a threat to the local population. Figure 9 shows another slope of a similarly unstable type in Wudu County. Here, large swathes of land have been reclaimed for agriculture use over the past few decades. The hillside has become aerated. These agricultural activities have been accompanied by the higher deformation rates caused by the Wenchuan earthquake, causing effects similar to those enhanced

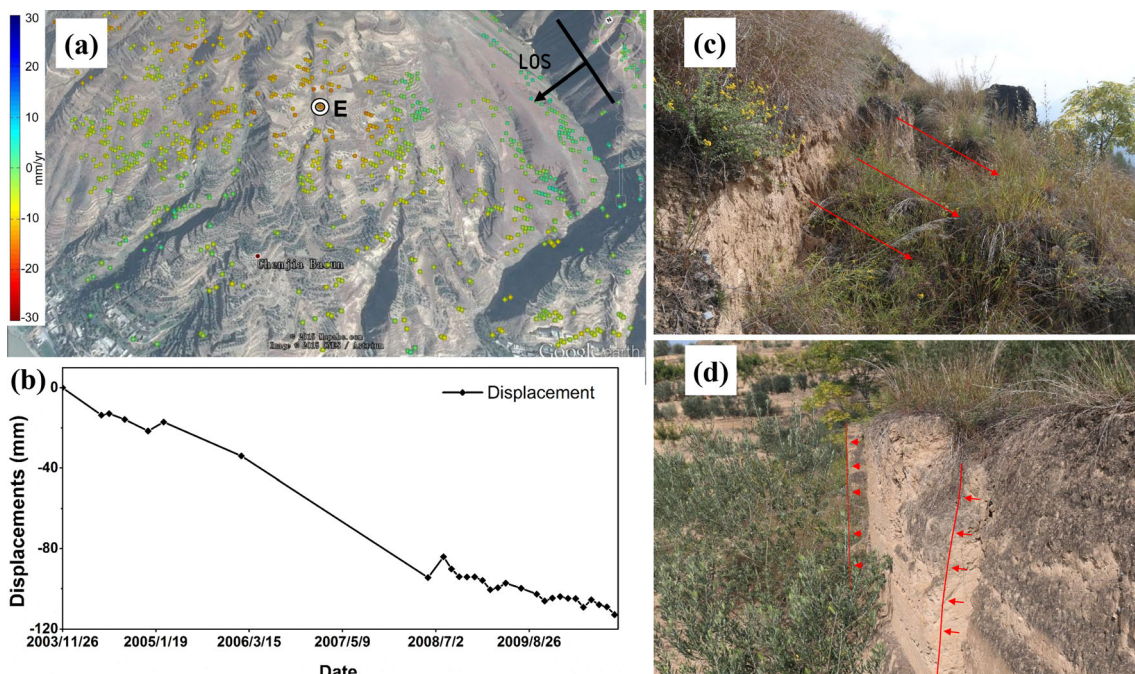


**Fig. 9** Displacement rates and damage caused by arable land cultivation. (a) Mean LOS displacement rates for SDFP pixels superimposed on Google Earth map; (b) Displacement time series for representative pixels, for Point E; (c, d) Examples of damage to a slope discovered during field surveys



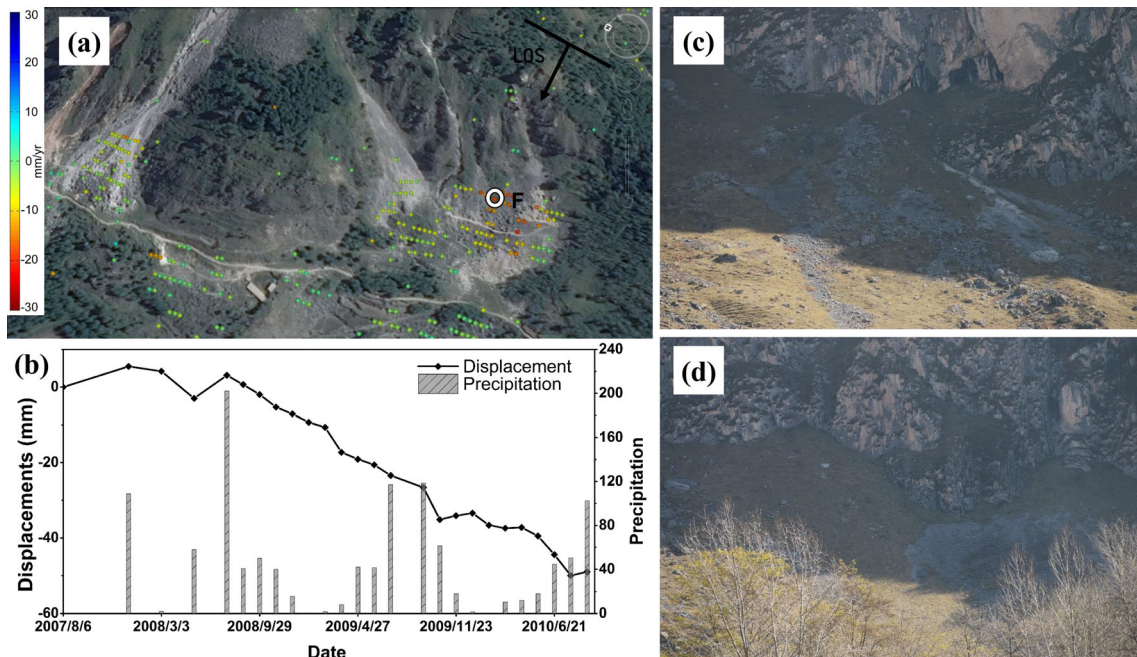


**Fig. 10** Displacement rates and photographic documentation of debris. (a) Mean LOS displacement rates for SDFP pixels superimposed on Google Earth map; (b) Displacement time series for representative pixels, for Point F; (c, d) Examples of debris discovered during field surveys

by poorly engineered road construction (Fig. 9b). The loose, cultivated soil and the intra-field channels and ridges built to aid water distribution have allowed rain to permeate the soil and increase its moisture content, which has also reduced the soil's shear strength and led to further deformation of the slope. Figure 9c and d show the cracks discovered on slopes during field surveys.

#### Debris

Landslides of natural terrain triggered by periods of intense rainfall are usually accompanied by debris flows. In the mountains, a torrent can cause the collapse of landslide dams, and a large debris flow can therefore form very rapidly (Cui et al. 2013). In the Bailong River Basin, weakened strata, tectonic activity (e.g., earthquakes, faulting) and precipitation can trigger landslide-deposited

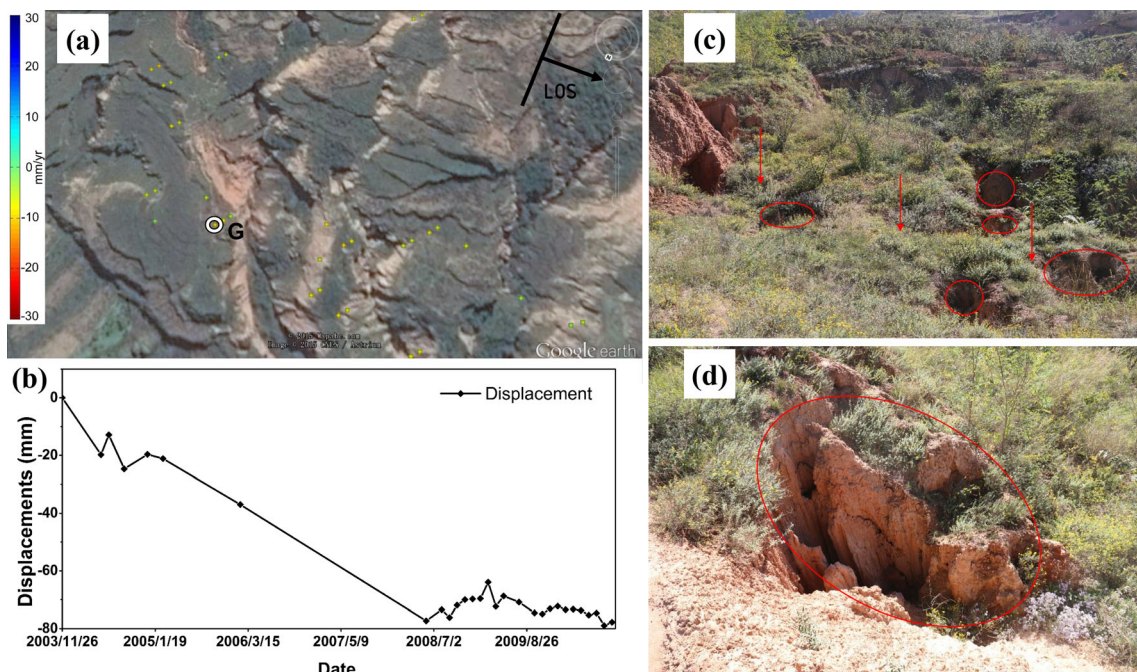


**Fig. 11** Displacement rates and photographic documentation of natural subsidence. (a) Mean LOS displacement rates for SDFP pixels superimposed on Google Earth map; (b) The displacement time series for representative pixels, for Point G; (c, d) Examples of subsidence and sink holes discovered during field surveys

materials to collapse into mountain gullies. Such movement continues with further precipitation. During periods of intense rainfall, flash floods form quickly, thus eroding some loose sediment in gullies, and these floods rapidly become debris flows. We therefore classified loose material deposited by landslides and subsidence/collapses that may become part of a debris flow as *debris*. Such material, especially if containing high volumes of stones, renders high SDFP pixel densities. Such loose material can deform at an accelerated rate of  $>20$  mm/yr in an away-from-LOS direction. Figure 10 shows such an example. This area is located in Zhouqu County (in the Bailong River's upstream). Here, the exposed rock and slope collapsed as a result of long-term weathering and rainfall, creating a massive sediment body at the foot of the slope (Fig. 10c, d). But further movement of the loosened material was enhanced by rainfall rates. Serious deformation occurred after episodes of intense rainfall (Fig. 10b).

### Subsidence

In the Bailong River Basin, there are two types of subsidence: natural and architectural.

Natural subsidence is related to the presence of soft soil-like sediments and loess and/or weak bedrocks. Figure 11 shows an example of such natural subsidence. The subsidence-affected displacement rate was  $>5$  mm/yr. This area in Wudu County is in the Bailong River's mid-stream area. Figure 11b shows the displacement time series of the slope (Fig. 11a) based on representative SDFP pixels. Substantial displacement was recorded

prior to May 28, 2008, with mean displacement rates returning to near-0 thereafter. Figures 11c and d show examples of the subsidence in the red mudstone bedrock illustrated by Figure 11a. It is characterized by a bedrock of red mudstone overlain by loess deposits and the red mudstone is heavily weathered. Rainfall had infiltrated the soil through cracks in the red mudstone and loess, creating numerous sink holes. Cavities within the soil caused by erosion combined with gravity led to subsidence on the slope's surface.

Artificial topographical mapping reveals that most buildings were built on landslide deposits and/or alluvial fans. Figure 12 shows an example of architectural subsidence in a building constructed on landslide deposits. Here, the sediment consisted of soft soils (sand, sandy silt, complex colluvial soils, etc.). Figure 12b shows how easily intense rainfall can cause subsidence in such soils. These areas display high SDFP pixel densities due to the dense clustering of buildings. The subsidence of the colluvial soils resulted in a variable cracking in the walls of buildings (Fig. 12c and d).

### Conclusions

The SBAS technique was used to detect ground deformation in the Bailong River Basin. Fifty-five C-band images covering the period between November 2003 to September 2010, from both upstream and downstream areas, allowed the successful identification of dangerous areas with high displacement rates.

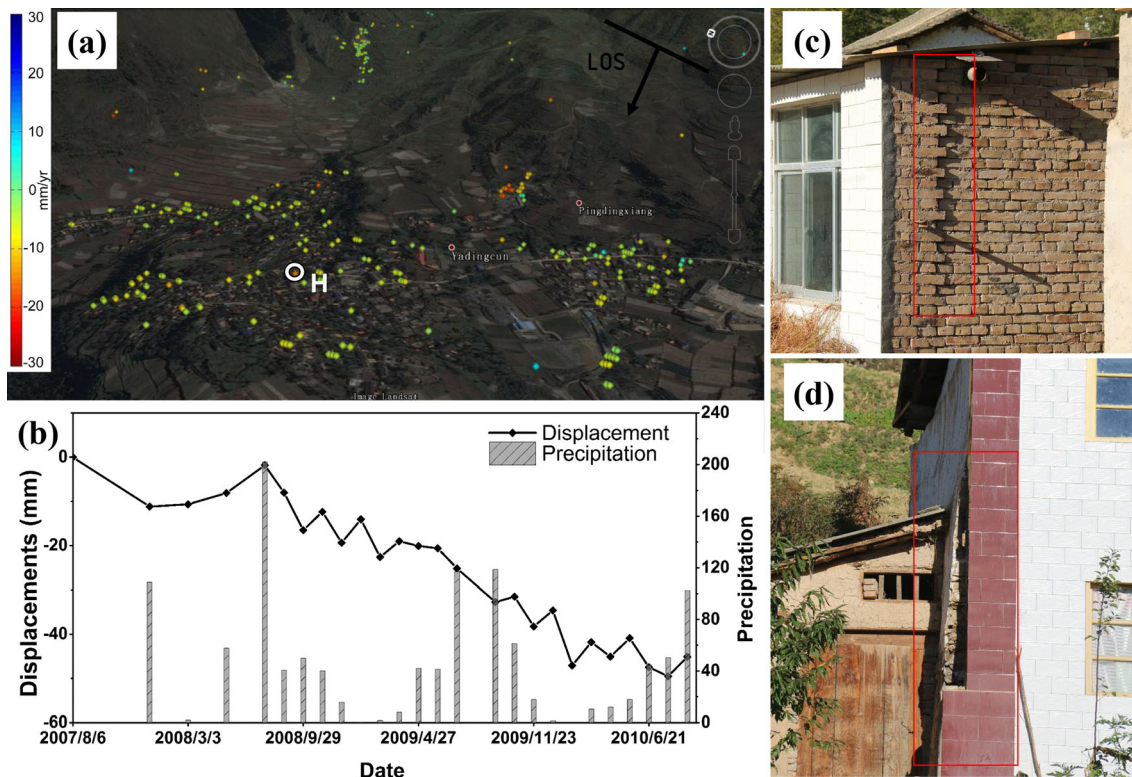


**Fig. 12** Displacement rates and photographic documentation of building subsidence. (a) Mean LOS displacement rates for SDFP pixels superimposed on Google Earth map; (b) Displacement time series for representative pixels, for Point H; (c, d) Examples of cracks in walls discovered during field surveys



Results from using the SBAS technique confirm that this method was useful in the accurate detection of the deformation of different topographies in the Bailong River Basin. The majority of SDFP pixels are distributed around the river valley itself, with high SDFP pixel densities caused by buildings and exposed rocks. Combining such results with landslide records and field survey data, the anomalous areas investigated using SBAS can be classified into three principal categories: landslides, debris, and subsidence. Displacement rates of up to 35 mm/yr were evaluated along the LOS. InSAR results show that this technique can capably analyze any displacement effect and successfully identify areas in the basin earmarked by field surveys as dangerous for human habitation. Deformation time series confirm that rainfall is a principal trigger of ground instability. Additionally, the Wenchuan earthquake seriously affected slope stability in the Bailong River Basin.

A successful application of the SBAS technique thus allowed the identification and confirmation of extensive areas of unstable landslides, debris deposits, and slopes within the Bailong River Basin. This constitutes a significant step in the prevention and reduction, of geohazards in this disaster-prone region.

Deficiencies in the technique were also apparent. The use of C-band analysis means that the method is perhaps better suited to the evaluation of slow/low displacement rates rather than sudden/large movements. The sensor's relatively small angle of incidence (proximate to a N-S direction) leads to insensitivity in the N-S displacement component; its low spatial resolution causes lower PS densities. These limitations could be effectively countered in the future by the use of new InSAR techniques employing with high spatial and temporal resolution imaging of the same region.

### Acknowledgments

This study was supported by the International S&T Cooperation Program of China (ISTCP) (Grant No. 2013DFE23030), the National Key Technology R&D Program of China (Grant No. 2011BAK12B06), the Fundamental Research Funds for the Central Universities (lzujbky-2015-133), and the National Natural Science Foundation of China (No. 41172328). The ENVISAT images were provided by the European Space Agency (ESA) to aid geohazard assessments of the Bailong River Basin, and radar data processing was carried out by Hooper et al. We would like to thank Tan Long, Guo Peng, Wang Siyuan, and Cui Zhijie for their assistance given during the study. We are grateful to the reviewers and editor for their constructive comments vis-à-vis improving the manuscript.

### References

Akbarimehr M, Motagh M, Haghshenas M (2013) Slope stability assessment of the Sarcheshmeh landslide, Northeast Iran, investigated using InSAR and GPS observations. *Remote Sens* 5(8):3681–3700

Bai S-b, Wang J, Zhang Z, Cheng C (2012) Combined landslide susceptibility mapping after Wenchuan earthquake at the Zhouqu segment in the Bailongjiang Basin, China. *Catena* 99:18–25

Bai S-b, Cheng C, Wang J, Thiebes B, Z-g Z (2013) Regional scale rainfall- and earthquake-triggered landslide susceptibility assessment in Wudu County, China. *J Mount Sci* 10(5):743–753

Berardino P, Fornaro G, Lanari R, Sansosti E (2002) A new algorithm for surface deformation monitoring based on small baseline differential SAR interferograms. *IEEE Trans Geosci Remote Sens* 40:2375–2383

Casu F, Manzo M, Lanari R (2006) A quantitative assessment of the SBAS algorithm performance for surface deformation retrieval from DInSAR data. *Remote Sens Environ* 102(3):195–210

Chen G, Meng X, Tan L, Zhang F, Qiao L (2014) Comparison and combination of different models for optimal landslide susceptibility zonation. *Q J Eng Geol Hydrogeol* 47(4):283–306

Ciampalini A, Bardi F, Bianchini S, Frodella W, Del Ventisette C, Moretti S, Casagli N (2014) Analysis of building deformation in landslide area using multisensor PsInSAR™ technique. *Int J Appl Earth Obs Geoinf* 33:166–180

Colesanti C and Wasowski J (2004) Satellite SAR interferometry for wide-area slope hazard detection and site-specific monitoring of slow landslides. In *Proceedings Ninth Internat. Symposium on Landslides* pp 117–125

Colombo A, Mallen L, Pispico R, Giannico C, Bianchi M and Savio G (2006) Mappatura regionale delle aree monitorabili mediante l'uso della tecnica PS. *Proceedings of 10 National Conference ASITA, Bolzano, Italy*, pp 14–17

Cui P, Zhou GG, Zhu X and Zhang J (2013) Scale amplification of natural debris flows caused by cascading landslide dam failures. *Geomorphology* 182:173–189

Dai F, Lee C, Ngai YY (2002) Landslide risk assessment and management: an overview. *Eng Geol* 64(1):65–87

Dijkstra T, Chandler J, Wackrow R, Meng X, Ma D, Gibson A, Whitworth M, Foster C, Lee K and Hobbs P (2012) Geomorphic controls and debris flows—the 2010 Zhouqu disaster, china. *Proceedings of the 11th International Symposium on Landslides (ISL) and the 2nd North American Symposium on Landslides*.

Ferretti A, Prati C, Rocca F (2000) Nonlinear subsidence rate estimation using permanent scatterers in differential SAR interferometry. *IEEE Trans Geosci Remote Sens* 38(5):2202–2212

Ferretti A, Prati C, Rocca F (2001) Permanent scatterers in SAR interferometry. *IEEE Trans Geosci Remote Sens* 39(1):8–20

Gabriel AK, Goldstein RM, Zebker HA (1989) Mapping small elevation changes over large areas: differential radar interferometry. *J Geophys Res Solid Earth* 94(B7):9183–9191

Hanssen RF (2005) Satellite radar interferometry for deformation monitoring: a priori assessment of feasibility and accuracy. *Int J Appl Earth Obs Geoinf* 6(3):253–260

Hooper A (2008) A multi-temporal InSAR method incorporating both persistent scatterer and small baseline approaches. *Geophys Res Lett* 35(16)

Hooper A, Zebker HA (2007) Phase unwrapping in three dimensions with application to InSAR time series. *J Opt Soc Am A* 24(9):2737–2747

Hooper A, Zebker H, Segall P, Kamps B (2004) A new method for measuring deformation on volcanoes and other natural terrains using InSAR persistent scatterers. *Geophys Res Lett* 31(23)

Hooper A, Bekaert D, Spaans K, Arkan M (2012) Recent advances in SAR interferometry time series analysis for measuring crustal deformation. *Tectonophysics* 514–517:1–13

Jiang X-Z and Wen B-p (2014) Creep behavior of the slip zone of a giant slow-moving landslide in northwest china: The suoertou landslide as an example. *Landslide Science for a Safer Geoenvironment*, Springer, pp 141–145

Kamps BM and Adam N (2003) Velocity field retrieval from long term coherent points in radar interferometric stacks. *Geoscience and Remote Sensing Symposium, 2003. IGARSS'03. Proceedings. IEEE 2003 International 2: 941–943*

Li Z, Zou W, Ding X, Chen Y, Liu G (2004) A quantitative measure for the quality of InSAR interferograms based on phase differences. *Photogramm Eng Remote Sens* 70(10):1131–1137

Liu G, Jia H, Zhang R, Cen M and Zhang T (2010) Subsidence detection by PS-InSAR based on high resolution Terrasar-X images. *Progress in Electromagnetics Research Symposium Proceedings Xi'an: Is n*, pp 11–15

Massonnet D, Feigl KL (1998) Radar interferometry and its application to changes in the Earth's surface. *Rev Geophys* 36:441–500

Meisina C, Zucca F, Notti D, Colombo A, Cucchi A, Savio G, Giannico C, Bianchi M (2008) Geological interpretation of PSInSAR data at regional scale. *Sensors* 8(11):7469–7492

Michoud C, Baumann V, Derron M-H, Jaboyedoff M and Lauknes TR (2015) Slope instability detection along the national 7 and the potrerillos dam reservoir, Argentina, using the Small-Baseline InSAR technique. *Engineering geology for society and territory-volume 2*, Springer, pp 295–299

Motagh M, Beavan J, Fielding EJ, Haghshenas M (2014) Postseismic ground deformation following the September 2010 Darfield, New Zealand, earthquake

- from Terrasar-X, CosMo-SkyMed, and Alos InSAR. *IEEE Geosci Remote Sens Lett* 11(1):186–190
- Peltier A, Bianchi M, Kaminski E, Komorowski JC, Rucci A, Staudacher T (2010) PslInSAR as a new tool to monitor pre-eruptive volcano ground deformation: Validation using GPS measurements on Piton de la Fournaise. *Geophys Res Lett* 37(12)
- Schlögel R, Doubre C, Malet J-P, Masson F (2015) Landslide deformation monitoring with ALOS/PALSAR imagery: a D-InSAR geomorphological interpretation method. *Geomorphology* 231:314–330
- Stramondo S, Bozzano F, Marra F, Wegmuller U, Cinti F, Moro M, Saroli M (2008) Subsidence induced by urbanisation in the city of Rome detected by advanced InSAR technique and geotechnical investigations. *Remote Sens Environ* 112(6):3160–3172
- Van Westen CJ, Castellanos E, Kuriakose SL (2008) Spatial data for landslide susceptibility, hazard, and vulnerability assessment: an overview. *Eng Geol* 102(3):112–131
- Zhao C, Lu Z, Zhang Q, de la Fuente J (2012) Large-area landslide detection and monitoring with Alos/Palsar imagery data over Northern California and Southern Oregon, USA. *Remote Sens Environ* 124:348–359

---

**Y. Zhang · X. Meng · G. Chen · L. Qiao · R. Zeng**

Gansu Environmental Geology and Geohazards Engineering Research Centre, College of Earth and Environmental Sciences, Lanzhou University, Lanzhou, 730000, People's Republic China

**Y. Zhang · X. Meng (✉) · G. Chen · L. Qiao · R. Zeng · J. Chang**

College of Earth and Environmental Sciences, Lanzhou University, Lanzhou, 730000, People's Republic China  
e-mail: xmmeng@lzu.edu.cn